

Structure of the Silica Phase Extracted from Silica/(TPA)OH Solutions Containing Nanoparticles

David D. Kragten, Joseph M. Fedeyko, Kaveri R. Sawant, Jeffrey D. Rimer,
Dionisios G. Vlachos,* and Raul F. Lobo*

Center for Catalytic Science and Technology, Department of Chemical Engineering, University of Delaware,
Newark, Delaware 19716

Michael Tsapatsis

Department of Chemical Engineering, University of Massachusetts, Amherst, Massachusetts 01003

Received: April 24, 2003; In Final Form: June 27, 2003

Subcolloidal particles of a few nanometers in diameter are observed during the clear-solution synthesis of silicalite-1. These nanoparticles (3–5 nm) can be synthesized at room temperature starting from tetrapropylammonium (TPA) hydroxide, tetraethyl orthosilicate (TEOS), and water, and they have been reported to have a uniform structure identical to that of zeolite ZSM-5 (called *nanoblocks* or *nanoslabs*). To study their structure, we followed the extraction procedure proposed in the literature to obtain a dry powder of the particles. These dried particles were analyzed with powder X-ray diffraction (XRD), solid-state NMR spectroscopy, FTIR spectroscopy, thermogravimetric analysis, and N₂ adsorption isotherms. The results are compared with those obtained for colloidal size silicalite-1, amorphous silica, and the mesoporous silicate SBA-15. To obtain a better idea of the shape and structure of the particles, we conducted simulated annealing modeling to fit the particle shape to the fractions of Qⁿ obtained from the ²⁹Si MAS NMR spectra. The model structures are in excellent agreement with our NMR data and suggest a poorly defined particle shape, in contrast to previous reports. The XRD patterns of samples with particle sizes in the range of the nanoparticles were simulated using the Debye formula and the SKIP algorithm. These simulations were carried out using structural models of silicalite-1 nanocrystals, the proposed nanoblock structure, and the silica particles derived from simulated annealing. We found no evidence in support of a well-defined MFI-like structure in the extracted material. The particles contain TPA, partly associated with the particles and partly as (TPA)Cl formed by the extraction process. The evidence accumulated here is in disagreement with the well-defined structure of the nanoparticles previously reported.

Introduction

The self-assembly of organic–inorganic hybrid materials is a subject of considerable research activity^{1–3} as it is important in the synthesis of composites with enhanced mechanical and electronic properties, novel biomaterials,⁴ biomineralization,^{5,6} and new porous catalysts^{7–12} and is a fundamental physico-chemical problem per se.^{13–16} The synthesis, nucleation, and crystal growth of high-silica zeolites epitomize some of the crucial phenomena that are encountered in the self-assembly of complex materials.^{14,17} In this case an organic structure director—such as tetrapropylammonium hydroxide or (TPA)-OH—is mixed with a silica source—tetraethyl orthosilicate, TEOS—and water. After a period of ~1 h, this uniform mixture is heated to ~100 °C and after a few hours yields high-quality crystals of a siliceous zeolite (silicalite-1, [(C₁₂H₂₈N⁺ OH[−])₄](SiO₂)₉₆—MFI).¹⁸

This so-called clear-solution synthesis of silicalite-1 has been investigated in detail by various groups.^{19–28} Because this synthesis is compositionally simple, highly reproducible, and amenable to detailed investigations using a battery of techniques, it has become a model system for fundamental research in

zeolite nucleation and crystal growth. The most general finding has been that previous to the observation of any crystals, the silica–(TPA)OH–water mixture rapidly microsegregates, forming two metastable phases: a *continuous* water-rich phase containing most of the water, a fraction of the (TPA)OH and a small amount of silica, and a *discontinuous* silica-rich phase that is observed in the form of uniform nanoparticles of ~3–5 nm.^{18,24,25} These nanoparticles have been observed by many groups: understanding their structure, potential of interaction, and dynamic properties are prerequisites to developing an atomic-scale model for zeolite nucleation and growth.²¹

Martens and collaborators have recently investigated the structure, formation, and evolution of these nanoparticles at high concentrations of silica and (TPA)OH.^{29–36} They have developed a method for the extraction of these nanoparticles from solution and used the characterization of the extracted material to conclude that the observed nanoparticles are highly uniform, well-defined units (called *nanoblocks* or *nanoslabs*)²⁹ with a very specific structure and geometry.³⁷ Their analysis of the nanoparticles leads to the conclusion that these nanoblocks are themselves small units of the MFI framework-type of ~1.3 × 4.0 × 4.0 nm in size. A reproduction of the putative structure of the nanoparticles is depicted in Figure 1.²⁹ This finding is potentially momentous as not only zeolites but many other

* Corresponding authors. R.F.L.: fax, (302)831-2085; e-mail, lobo@che.udel.edu. D.G.V.: e-mail, vlachos@che.udel.edu.

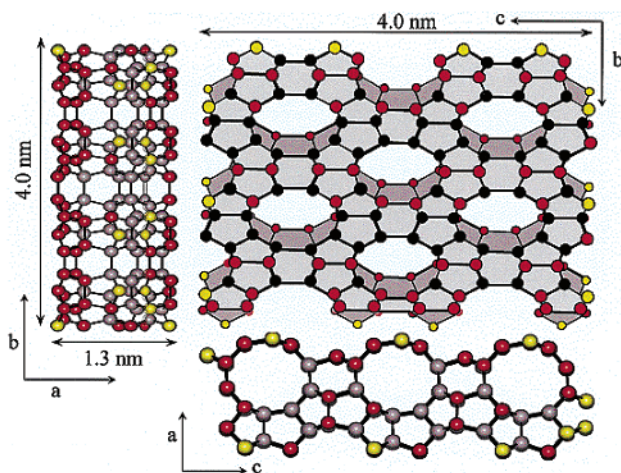


Figure 1. Proposed structure of subcolloidal zeolite precursor nanoparticles. From ref 29. Crystallographically oriented elementary "nanoslab" of silicalite-1. The Q^4 , Q^3 , and Q^2 type T-atoms are denoted as black, red, and yellow spheres, respectively. The figure shows three views of the nanoslabs along the three crystallographic directions.

materials might be formed through similar routes.³⁸ Building upon the analysis of the extracted material from solution, a rather detailed model for the formation of the nanoblocks has been proposed and a detailed process for the actual assembly of zeolite crystals using the nanoblocks as building units has been put forward by the same group.^{32–36}

Given the potential value of this discovery, we have reinvestigated in detail the structure of the extracted material from the nanoparticles suspension and compared our results to the measurements originally reported in ref 29. Our analyses lead to conclusions that are diametrically opposed to the results reported by Martens et al.²⁹ We have found no evidence indicating that the local structure of the extracted material resembles the structure of the MFI framework-type.

Experimental Section

To compare XRD patterns and solid-state NMR spectra of various forms of silica, we have prepared several samples with selected structures and particle sizes. In this section we first describe the synthesis and separation protocol of the nanoparticles. Then we describe the synthesis of larger colloidal, crystalline particles (both silicalite-1 and ZSM-5) and of mesoporous SBA-15 silica. Amorphous silica from commercial sources has also been used.

Nanoparticle Synthesis and Extraction. The nanoparticles were synthesized and extracted from a clear aqueous solution according to the method proposed by Ravishankar et al.³⁷ In a plastic beaker, 7.8 g of tetrapropylammonium hydroxide ((TPA)-OH, Alfa Aesar, 40 wt % in water) and 9.0 g of tetraethyl orthosilicate (TEOS, Aldrich, 98%) were mixed for several minutes, followed by the dropwise addition of 9.0 g of deionized water with vigorous stirring. The mixture was stirred at room temperature until it became clear (about 4 h). We refer to this solution as TPA-silicalite solution. (In the original publication^{29,37} the mixture is stirred for 24 h. However, we found no difference in the particle size and the extracted product when the samples were stirred for 4 h instead of 24 h.) The particles are extracted as follows: to start, 7 mL of the TPA-silicalite solution was added dropwise to a vigorously stirred 15 mL solution of 0.5 N HCl (Sigma, 36.7 wt %, 99%). All solutions were cooled in an ice-bath prior to mixing. Then, 5 mL of the acid solution was added to 15 mL of THF (EM Science, 99.5%),

and the solution was mixed. NaCl (Alfa, 99%) was added in small amounts until a clear phase separation was observed. The organic layer was removed and the acid solution was extracted several more times. The THF, containing the particles, was evaporated in a rotavap under reduced pressure at 60 °C, yielding a white powder as product. During all stages of the separation, the solution was clear. An additional purification step was performed in selected cases by washing the powder with deionized water.

Synthesis of Colloidal Silicalite-1 and ZSM-5 Particles.

Samples of the siliceous form of ZSM-5 (also called silicalite-1) were synthesized with different crystal dimensions from clear solution by hydrothermal methods. The following stoichiometry was used: 10 SiO_2 :5 (TPA)OH:300 H_2O :40 EtOH. This composition was obtained by mixing 25.75 g of deionized water and 5.25 g of (TPA)OH (Alfa Aesar, 40 wt %) in a plastic beaker, followed by adding dropwise 10.0 g of TEOS (Aldrich, 98%), with vigorous stirring. Stirring was continued until the solution became clear (about 2–3 h). The solution was then placed in a Teflon-lined stainless steel Parr autoclave and heated at 130 °C under rotation for 5 to 8 h. The autoclave was then quenched in water and the product was filtered and washed with deionized water until the pH was lower than 8. The particles were separated by centrifugation. The washing step removed all excess TPA. After air drying, a white powder was obtained of about 300 nm colloidal silicalite-1 particles.

Smaller colloidal particles were obtained from a gel with composition 10 SiO_2 :2.4 (TPA)OH:1 NaOH:110 H_2O :40 EtOH, following the procedure of Lovaglio et al.³⁹ The gel was obtained by dissolving 0.43 g of NaOH (Fisher Scientific, 98.1%) in 30 mL of (TPA)OH (Alfa Aesar, 40 wt %). After adding 7.5 g of fumed silica (Cab-O-Sil M5, Cabot Corp.), the slurry was heated at 80 °C until a clear solution was obtained. The gel was hydrothermally treated in a Teflon-lined autoclave at 125 °C under rotation for 8 h. Purification was identical to that of the aforementioned silicalite-1 colloidal particles. Typically, particles of about 100 nm were obtained.

ZSM-5 (Si/Al = 28) crystals were also obtained from a gel with composition 94 SiO_2 :10 (TPA)Br:3 NaAlO_2 :34 NaOH:4440 H_2O . The gel was prepared by dissolving 1.36 g of NaOH (Fisher Scientific, 98.1%) and 0.25 g of sodium aluminate ($\text{NaAlO}_2 \cdot 0.24\text{H}_2\text{O}$, EM Science) in 80.0 g deionized water. Next, 2.66 g of (TPA)Br (Aldrich, 98%) was added to the liquid and finally, 6.0 g of fumed silica (Cab-O-Sil M5, Cabot Corp.) was added. The synthesis solution was stirred for about 2 h. Hydrothermal treatment in a Teflon-lined autoclave for 6 days at 160 °C under static conditions yielded white crystals that were further washed with deionized water. The Si/Al ratio is 27.9 on the basis of elemental analysis (Galbraith Laboratory, Inc.).

Mesoporous Silica. SBA-15 is an ordered mesoporous silicate with cylindrical pores in hexagonal close-packed arrangement. The silica walls between the pores have a thickness of 31–64 Å and are amorphous.⁴⁰ This structure is very open, giving rise to very large surface areas and pore volumes.

SBA-15 silica was synthesized following a procedure adapted from refs 41 and 42. A 4.0 g sample of Pluronic P123 triblock copolymer ($\text{EO}_{20}\text{PO}_{70}\text{EO}_{20}$, $M_{\text{av}} = 5750$, BASF) was dissolved in 97.1 g of water and 19.08 g of a 37 wt % HCl solution at 35 °C. Then, 8.50 g of TEOS was added and kept at 35 °C for 20 h with stirring. The low-temperature preparation was followed by aging overnight at 80 °C using static conditions. The solid product was filtered, washed with ample deionized water, and dried at room temperature. Calcination was carried out by slowly

ramping the temperature to 300 °C in 5 h and was continued by heating at 300 °C for another 12 h. Successively, the dried powder was treated with (TPA)OH by adding a small amount of (TPA)OH/glycerol to the SBA-15, just enough to wet it, followed by drying in air. SBA-15 treated in this manner is referred to as TPA-SBA-15. Further details on the synthesis and characterization of this sample are reported elsewhere.⁴³

Amorphous Silica. The amorphous silica phases we used are fumed silica Cab-O-Sil M5 (Cabot Corporation) and precipitated silica Ultrasil VN3 (Degussa Corp.).

Analytical Section

Dynamic light scattering (DLS) measurements were obtained using a Brookhaven Instruments BI9000AT correlator and BI200SM goniometer. The samples were placed in a Decalin index-matching bath and were illuminated with a 488 nm laser source (Lexel 95 2 W Ar laser). All measurements were performed at 25 °C and a scattering angle of 90°. The intensity autocorrelation function was analyzed using a CONTIN regression method for the nanoparticles, whereas a cumulant method was utilized to obtain the size and polydispersity of the larger colloidal particles. Prior to measurement, the samples were syringe-filtered through a hydrophilic membrane (Supor, Pall Gelman) of the appropriate pore size to remove dust particles. The nanoparticle solution was directly measured using a 0.45 μm membrane filter, while colloidal particles were first dispersed in deionized water by sonification, and then filtered with a 0.80 μm membrane.

Powder X-ray diffraction (XRD) patterns were measured using a Philips X'Pert X-ray diffractometer (Cu K α radiation). Scattering intensity was measured in reflection mode from $2\theta = 0.5$ to 100° with a step size of 0.02° and 35 s per step. FTIR spectra were recorded using the KBr pellet technique ($\sim 1\%$ w/w) with a Nicolet 510 IR spectrometer. The spectra were collected in absorption mode from 400 to 4000 cm^{-1} at room temperature under nitrogen (256 scans). The calibration of the spectrometer was verified by comparing the shift of bands characteristic of atmospheric CO₂ with literature values. Thermogravimetric analyses (TGA) were conducted using a Cahn TG-121 microbalance with a heating rate of 2 K/min from room temperature to 1070 K. Nitrogen adsorption isotherms were obtained at 77 K using a Micromeritics ASAP 2010 adsorption instrument. The samples were evacuated at various temperatures and times prior to the measurement. The BET specific surface area was evaluated in the relative pressure range $0.04\text{--}0.2P/P_0$. The density of liquid nitrogen was taken as 0.029 mol/mL .

²⁹Si and ¹³C{¹H} solid-state MAS and CP/MAS NMR spectra were recorded using a Bruker MSL 300 MHz spectrometer operating at resonance frequencies of 59.627 and 75.68 MHz, respectively. Chemical shifts are referenced to 3-(trimethylsilyl)-1-propanesulfonic acid (DSS) and hexamethylenbenzene (HMB), for ²⁹Si and ¹³C, respectively. The samples were spun in a 7 mm zirconia rotor at a spinning rate of 3 kHz. ²⁹Si MAS NMR spectra were acquired using a $4\text{ }\mu\text{s}$ $\pi/3$ pulse, high-power proton decoupling, and a 90 s recycle delay. ²⁹Si{¹H} CPMAS NMR spectra were acquired with a $6\text{ }\mu\text{s}$ ¹H $\pi/2$ pulse, a contact time of 3 ms, a recycle delay of 5 s, and high-power proton decoupling. ¹³C{¹H} CPMAS NMR spectra were recorded similar to ²⁹Si{¹H} CPMAS, with a contact time of 2 ms.

Simulations

Simulation of XRD Patterns from Small Particles. To simulate the XRD patterns of nanoparticles (which may or may not have translational symmetry due to their small size), XRD

patterns were calculated using the Debye scattering equation, i.e., by summation over the amplitude of scattering of all atomic pairs. The equation assumes that the particles are randomly oriented and that they are uncorrelated (i.e., there is no interference from the scattering of adjacent particles).⁴⁴ The scattering factors were evaluated according to the function and parameters suggested by Waasmaier.⁴⁵ There are no assumptions about any translational symmetry within the sample and thus arbitrary portions of a unit cell or combinations of unit cells can be used as models to calculate the diffraction pattern. Since these calculations are computationally intensive for large structures (a $2 \times 2 \times 2$ unit cells model takes about 14 h), another method was used to simulate the XRD patterns of nanoscale crystals. We implemented the SKIP algorithm,⁴⁶ as proposed by Schlenker et al.,⁴⁷ for nanocrystals larger than a few unit cells.⁴⁸ This algorithm computes the scattering from crystals of arbitrary size (but bigger than one unit cell), and peak broadening arises naturally from the calculations; peak broadening is not estimated by applying the Scherrer equation.⁴⁴ The limitation of SKIP is that the particles *must* have translational symmetry, and thus patterns for particles of arbitrary shape or without translational symmetry cannot be calculated. Both methods gave identical results for the same model structures.

Simulated Annealing. To analyze the ²⁹Si MAS NMR spectra—which have been used to infer the nanoparticle shape by Ravishanker et al.²⁹—we have adapted a systematic simulated annealing optimization method.^{49,50} In this technique nanoparticles composed of SiO₂ only are constructed on the computer and quenched slowly from sufficiently high temperatures. During the quenching process, the units (building blocks) making up the structure move according to certain rules and these moves are accepted using a Metropolis algorithm. Given its statistical mechanics basis, this method searches the phase space effectively and thermal fluctuations can drive the system uphill in energy (or uphill in any other objective function used) resulting in high probability of finding the global minimum, i.e., the structure that best fits the data. In this manner, unbiased solutions with possible nonregular geometric shapes can result.⁵¹ In addition to disordered initial structures,^{52,53} regular geometric shapes can also be used as initial structures and quenched from various initial temperatures. When the initial temperature is sufficiently low, the regular shapes can be “frozen” as local optimization minima and their objective function can be compared to those of nanoparticles that have been annealed properly. When the initial temperature is high, one can examine whether regular shapes can be maintained as the global minimum during the annealing process.

Since it has been proposed that the nanoparticle structure resembles the structure of crystalline silicalite-1, we have examined a subset of possible solutions that yield SiO_{4/2} units in the expected positions of the MFI framework-type. Two possible units were considered. First structures were built using a 12 T-atom building unit (the 12 T-atom asymmetric unit of the unit cell of silicalite-1), as shown in Figure 2a. Our approach parallels construction of zeolites from relatively large building blocks, where lattice energies are computed to compare their relative stability. It may be expected that when the building block is sufficiently large (e.g., comparable in size to the nanoparticle), the structure is already “dialed-in” with the building block and annealing has little influence on the results. To examine the effect of the size of the building block, we also considered using individual SiO_{4/2} tetrahedra as the building block. This is nearly the smallest unit (with the exception of single Si and O atoms).

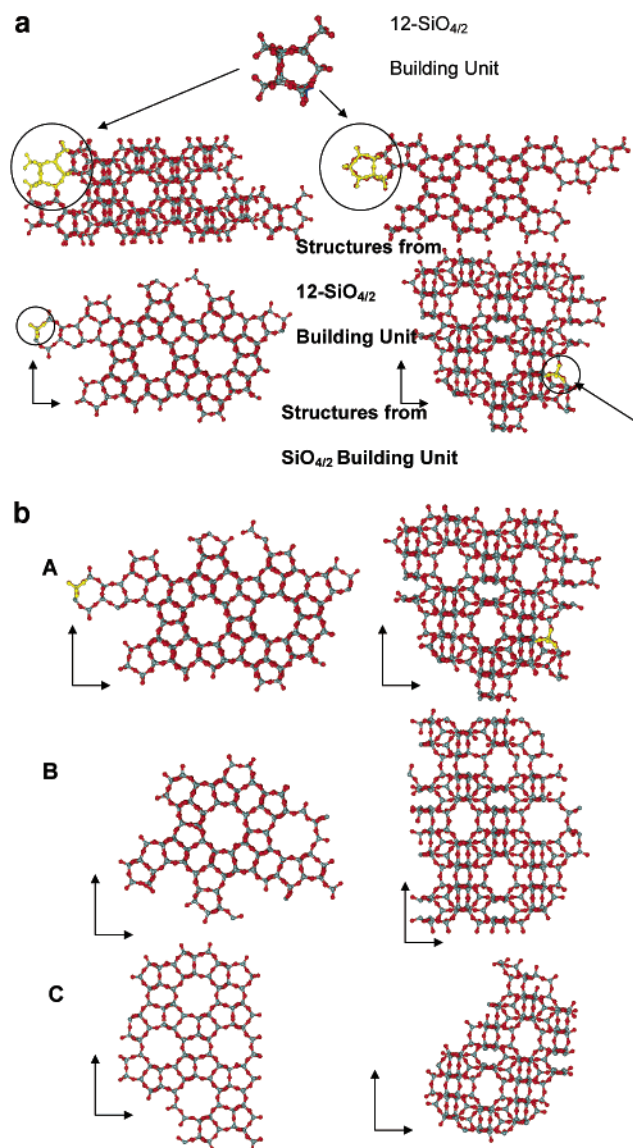


Figure 2. (a) Final structures obtained with simulated annealing by fitting ^{29}Si MAS NMR spectra obtained from the extracted nanoparticles. On the top, views of a structure modeled with the 12-T atom pentasil building block are shown, and on the bottom views of a structure modeled with the $\text{SiO}_{4/2}$ building block are shown. (b) Images of three structures minimized using the single $\text{SiO}_{4/2}$ building unit.

The moves of the units on the lattice are performed with a reaction kinetic Monte Carlo (KMC) type of simulation. In particular, at each temperature of the quenching process a number of moves of the building blocks are attempted. The moves consist of random diffusion events on the lattice with certain probabilities. For instance, a selected 12 T-atom unit can move to any of the eight symmetry related points in any of the unit cells of the simulation box (in addition to translations this may involve rotations and inversions of the building unit). During a potential new move, the set of all Q^n of the potential new structure is computed and compared to the experimental one. The Euclidian distance between experiment and simulation is the objective function for this problem. When the distance from the experimental Q^n values is reduced, the move is automatically accepted; otherwise it may be accepted by comparing the corresponding Boltzmann factor to a random number. During a simulation, the nanoparticle shape, radius of gyration, and the objective function are followed and graphed.

Regarding the annealing schedule, in most simulations the

initial temperature T_0 was varied between 400 and 20000 deg. The final results were nearly unaffected by the initial temperature, for $T_0 > 8000$. For $T_0 < 8000$, the temperature step size must be varied to ensure that the system reaches the optimum Q^n values. As an example, for $T_0 = 400$ temperature steps of around 0.1–0.3 deg are needed to reach good optima. The final temperature was varied from 10 to 200 deg, with optima appearing only below 50 deg. At each temperature, ~ 1000 Monte Carlo events were performed.

During the simulation of the nanoparticle from either building unit, the effect of simulation box size must be optimized to prevent the system from biasing the simulation. Large simulation boxes lead to multiple nuclei and result in fragmented particles. On the other hand, small simulation boxes bias the dimensions of nanostructures. Therefore, it is important that proper box sizes are used. In the 12 T-atom model, the effect of lattice size is negligible for simulation boxes greater than $10 \times 10 \times 10$ building units. For the total number of blocks in the system (~ 30), this lattice size corresponds to a solid density of $\sim 3\%$. Similarly, for the single silicon model, a lattice size of $18 \times 18 \times 18$ building units was required to ensure that the results are size independent (this represents a solid density of $\sim 5\%$). The bonding rules corresponding to both simulation boxes are based on the MFI framework topology, ensuring that the nanostructures have the MFI structure proposed in ref 29.

Results

Particle Size Evolution during the Separation Protocol.

During the synthesis and extraction of the nanoparticles, the evolution of the particle size was followed using DLS to observe any modification induced by the various steps of the extraction process. The hydrolysis of TEOS to form the nanoparticles is complete after approximately 4 h, and the particles do not appear to change in size for at least 24 h at room temperature. The particle size, obtained through CONTIN regression analysis, was within the range from 1 to 20 nm. The scattering intensities were low in all cases and it is difficult to obtain a precise size distribution of the nanoparticles with the available DLS instrument. However, the results indicate that the majority of particles are less than 10 nm, which agrees with previously reported values.¹⁹

The acidification of the synthesis solution by addition of HCl causes the nanoparticles to aggregate and form approximately 200 nm particles, as observed by DLS. These particles are then extracted into a THF phase, which is separated from the aqueous solution after the addition of NaCl. The extracted phase was analyzed with DLS, revealing particle sizes of approximately 500 nm, which are unstable and continue to grow over time. The particles, once dried, are difficult to redisperse in solution by sonification or pH changes through the addition of (TPA)-OH. In summary, DLS indicates that significant aggregation occurs during the extraction process. The aggregation may or may not alter the fundamental structure that nanoparticles have in solution, an issue discussed below.

XRD Patterns of Extracted Nanoparticles. XRD patterns of the extracted nanoparticles and amorphous silica are shown in Figure 3. The sharp peaks in the pattern of the extracted silica phase of nanoparticles are due to NaCl, which was not washed out sufficiently after the extraction. Washing with water removes the NaCl peaks completely while preserving the rest of the pattern. It is clear that the diffraction pattern of the extracted nanoparticles appears very similar to amorphous silica. For the nanoparticles, a number of broad peaks are located at about 7, 25, 47, 67, and 77° 2θ . The pattern of amorphous silica has

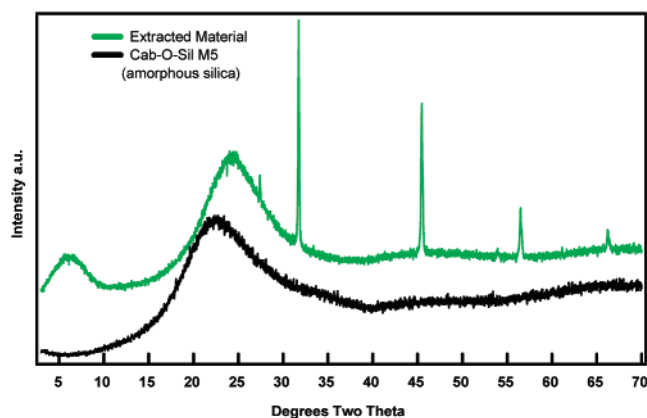


Figure 3. XRD patterns of amorphous silica (Cab-O-Sil) and extracted nanoparticles. The sharp peaks in the extracted nanoparticles are from the sodium chloride used during the extraction into THF.

similar peaks with only a small shift in the peak positions. The main difference between the two XRD patterns is the broad peak at $7^\circ 2\theta$ observed in the extracted material. Given that at higher angles the patterns are nearly identical, this is most likely a feature associated with particle size ($d \sim 12.7 \text{ \AA}$) and it is not related to the internal atomic structure of the extracted material (see XRD simulations below). The source of the amorphous silica does not affect the X-ray pattern significantly: both fumed (Cab-O-Sil) and precipitated silica (Ultrasil) give essentially the same XRD pattern. Note that not only the peak position, but also the intensity of the peaks is nearly the same for amorphous silica and the extracted nanoparticles. In contrast, we find that the position of the peak at lower angles—or larger d spacing—does vary considerably from phase to phase. For the nanoparticles, the position varies from sample to sample by a few degrees. This dependence on sample preparation is an indication that the peak is probably associated with particle size effects, rather than with the internal structure of the material. If this were the case, changes in this peak would be accompanied by changes at higher angles.

NMR Spectroscopy. From an analysis of ^{29}Si MAS NMR spectra, information about the connectivity of the silicate network can be obtained.⁵⁴ This is expressed by the fraction of Q^n , where n indicates the number of siloxane bonds and $4 - n$ gives the number of silanol groups ($\text{Si}-\text{OH}$). Q^4 , Q^3 , and Q^2 peaks are found at the expected chemical shifts of -112 , -103 , and -94 ppm , respectively.

In Figure 4 the ^{29}Si MAS NMR spectra of TPA-ZSM-5, silicalite-1, and extracted nanoparticles are shown. The peaks can be fitted with Gaussians to obtain the relative area of each peak (see Table 1); in the figure the components and the sum of the components for the extracted material are also depicted. We estimate that the error in the calculated areas is $\sim 2\%$ units of the absolute value. TPA-ZSM-5 contains few internal defects and the shoulder observed at $\sim -105 \text{ ppm}$ arises from the $\text{Si}(1\text{Al})$ signal⁵⁴ and not from the Q^3 signal (see FTIR results below). The silicalite-1 sample and the extracted nanoparticles are free of framework aluminum and here the relative proportion of Q^3 s and Q^2 s increases from silicalite-1 to nanoparticles as expected due to size. In particular, nanoparticles have a large portion of Q^3 s and a significant fraction of Q^2 s. Silicalite-1 has a substantial fraction of Q^3 because the charge of the TPA^+ cation is balanced by a siloxy group (SiO^-) and three silanols (SiOH).^{55–58} These silicalite-1 particles are too big to detect surface silanol groups.

$^{13}\text{C}\{^1\text{H}\}$ CPMAS NMR spectra of colloidal silicalite-1 and nanoparticles (not shown) confirm the presence of TPA. The

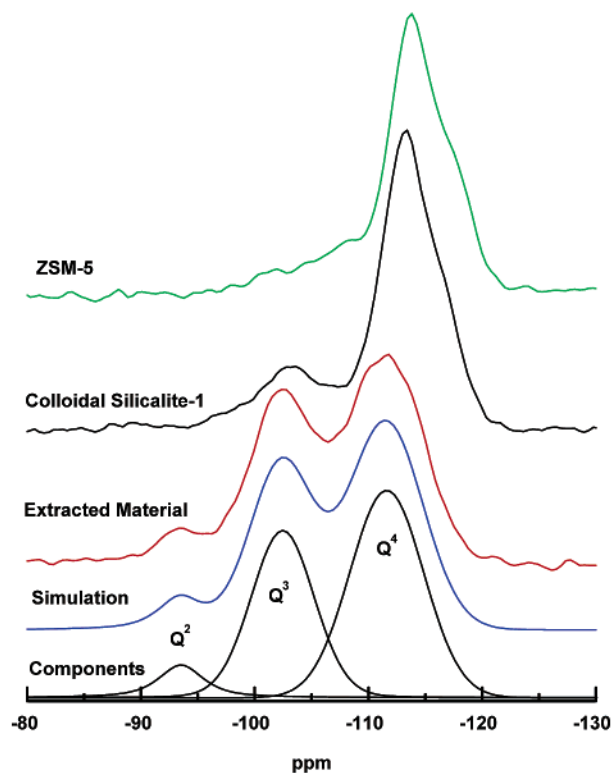


Figure 4. ^{29}Si MAS NMR spectra of ZSM-5, colloidal silicalite-1, and extracted nanoparticles. The bottom two traces are the components and the simulation of the spectrum of the nanoparticles.

TABLE 1: Relative Areas of the ^{29}Si MAS NMR Peaks of TPA-Containing Silicalite-1 and Extracted Nanoparticles

silica phase	fraction of Q^n groups (%) ^a		
	Q^2	Q^3 or $\text{Si}(1\text{Al})$	Q^4
silicalite-1 (300 nm)		10.1 (−103)	89.9 (−114)
extracted nanoparticles	6.4 (−94)	43.5 (−103)	50.1 (−112)
extracted nanoparticles ^b	8.3	40.6	51.1
ZSM-5		6.5 (−107)	93.5 (−114)

^a The peak positions in ppm are given in parentheses. ^b Literature values from ref 29.

spectra appear identical to that of TPA-containing ZSM-5.^{15,16} $^{29}\text{Si}\{^1\text{H}\}$ CPMAS NMR of the nanoparticles shows enhancement of the Q^3 peak in particular and to a lesser extent of the Q^2 peak. As shown in Table 1, the fraction of Q^2 , Q^3 , and Q^4 are identical to the ones reported by Ravisankar et al.^{29,31,37}

FTIR of Extracted Nanoparticles. From comparisons of FTIR spectra of samples of known structure with our samples, additional information can be obtained about the structure of the extracted materials. Different ranges of the spectrum provide local information related to different aspects of the structure.^{59–61} Spectra of ZSM-5, colloidal silicalite-1, nanoparticles (washed and unwashed), amorphous silica, and SBA-15 are shown in Figure 5. For the extracted material, most features are independent of the degree of washing, though TPA-related bands are less pronounced for a washed sample. A number of significant differences between the silica phases are apparent in a number of different regions of the spectrum.

The strongest band is observed in the asymmetric siloxane stretch ($\text{Si}-\text{O}-\text{Si}$) region, from about 950 to 1250 wave-numbers.^{60,62–64} In this region, the strongest band is at about 1090 cm^{-1} , and it is present for all samples.⁵⁹ At about 1220 cm^{-1} , a clear peak is observed for ZSM-5 and colloidal silicalite-1. In contrast, for amorphous silica, SBA-15, and the nanoparticles, only a broad shoulder is observed. Note that the skeletal

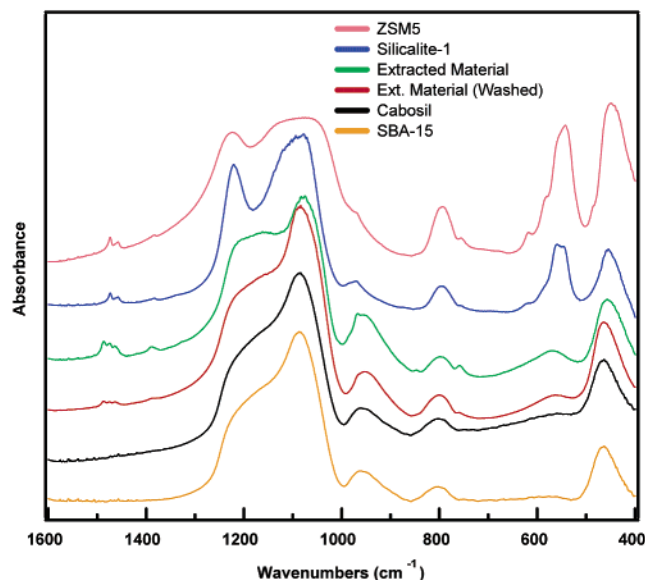


Figure 5. FTIR spectra of ZSM-5, colloidal silicalite-1, extracted nanoparticles, and extracted (and washed) nanoparticles, Cab-O-Sil and SBA-15. All spectra are scaled to the peak at about 450 wavenumbers.

modes ($950\text{--}1250\text{ cm}^{-1}$), for the amorphous silica, SBA-15, and the nanoparticles are nearly indistinguishable. In the region characteristic of the mode with prevailing silanol stretching character (Si-OH , $920\text{--}1020\text{ cm}^{-1}$),⁵⁹ band shape and intensity depend on the silica phase. A band at 950 cm^{-1} is clearly observed for amorphous silica, SBA-15, and the nanoparticles: this band is associated with a localized Si-OH stretching mode.⁵⁹ For ZSM-5 crystals this band is absent as the sample contains very few defects (internal SiOH).^{59,65} For silicalite-1 it is blue shifted to $\sim 960\text{ cm}^{-1}$.⁵⁹ This shift can be understood if we recall that in TPA-silicalite-1 this band corresponds to internal siloxi/silanol groups⁵⁸ needed to balance the charge of TPA^+ .⁵⁵ As the OH bond polarity increases upon hydrogen-bond formation (similar to a $\text{Si-O}^{\delta-}$),^{66,67} the stretching frequency is expected to increase. (Note that in sodium silicate glasses the band at 1090 cm^{-1} is attributed to a stretching mode of nonbridged Si-O^-).⁶⁸ A similar band is observed for the nanoparticles.

The symmetric vibrations of the Si-O-Si bonds are observed in the $750\text{--}850\text{ cm}^{-1}$ interval.^{59,62} This complex region is constituted of many overlapping components. In our case, this frequency depends on the silica phase and is blue shifted by a few wavenumbers when amorphous silica and the nanoparticles are compared with silicalite-1 and ZSM-5. A weak band at 751 to 754 cm^{-1} is observed for all silica phases, though it is much more pronounced for the nanoparticles (not washed). On the other hand, a weak band at about 842 cm^{-1} is only present for amorphous silica and the nanoparticles, where the latter is actually a shoulder of the 794 cm^{-1} band. Again this band is much more pronounced for the extracted material.

Large differences are seen in the $500\text{--}650\text{ cm}^{-1}$ region where the modes have been assigned to the double 5-ring (or a pentasil ring in the case of silicalite-1).⁶⁴ For amorphous silica and SBA-15, only a slight trace of a very weak, broad band is present at $\sim 565\text{ cm}^{-1}$. On the other hand, clear bands are observed for the crystalline phases: ZSM-5 (at about 540 cm^{-1}) and silicalite-1 (doublet at 542 and 556 cm^{-1}). For the extracted nanoparticles, a band rather similar to that of amorphous silica is observed. A broad weak-to-medium band is detected at $\sim 565\text{ cm}^{-1}$, blue shifted by about 25 wavenumbers from the sili-

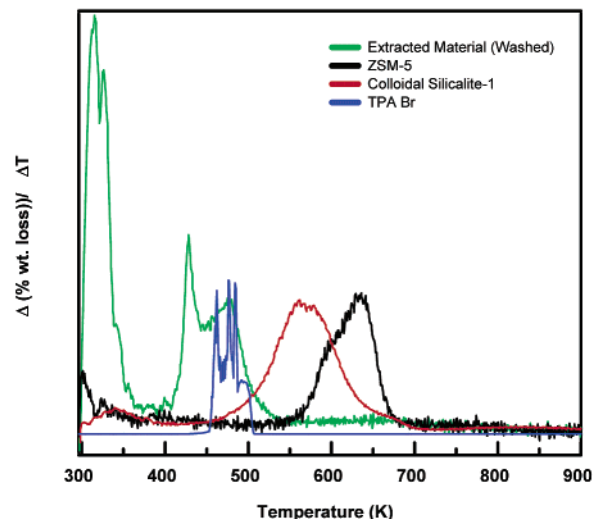


Figure 6. DTA traces of TPA-containing ZSM-5, colloidal silicalite-1, extracted nanoparticles, and (TPA)Br.

calite-1 phase. This band becomes weaker by washing the nanoparticles with water to remove excess TPA.

In the Si-O bending region, from about 420 to 500 cm^{-1} , a strong band is present at about 450 to 465 cm^{-1} . This band shifts slightly from one silica phase to the other: amorphous silica and the nanoparticles are blue shifted by about 10 wavenumbers in comparison with ZSM-5 and silicalite-1.

In the C-H bending region, from 1250 to 1530 cm^{-1} , a number of peaks are observed due to the presence of TPA.^{69,70} Since amorphous silica does not contain TPA, no bands are observed for Cab-O-Sil (and Ultrasil). Moreover, the more TPA is present, the more pronounced the bands appear. For both ZSM-5 and colloidal silicalite-1, two CH_3 deformation bands appear at 1456 and 1472 cm^{-1} ; only the former band is observed with Raman spectroscopy.^{63,69,70} Nanoparticles show, however, three bands in the region, at 1458 , 1471 , and 1483 cm^{-1} . The number of bands and positions are expected to be affected by the conformation(s) of the TPA molecule, which has been studied with Raman and NMR spectroscopies.^{71,72} The differences in the CH_3 deformation bands suggest that the conformation of the TPA molecules in the extracted nanoparticles differs from the conformation of TPA in silicalite-1. Only a trace of the CH_2 wagging mode is observed at 1320 cm^{-1} ; the Raman band has been observed at 1324 cm^{-1} . With Raman, a CH_2 wagging mode is observed at 1340 cm^{-1} , whereas we observe a band at 1384 cm^{-1} for the nanoparticles, ZSM-5, and silicalite-1. This very large shift could be rationalized by assigning the band to an asymmetric rather than a symmetric wagging mode. From differences primarily in the deformation mode range, we conclude that at least a large fraction of the TPA molecules in the extracted nanoparticles do not have the conformation of TPA in silicalite-1.

Thermogravimetric Analyses. Several weight-loss events are observed when the samples containing TPA are heated from about 373 to 900 K . The weight loss can be attributed to the decomposition and desorption of TPA byproducts and, to a lesser extent, the desorption of water released by the condensation of silanol groups within the silica. Nearly all bulk water desorbs by about 373 K . Above 373 K , weight losses occur at two distinct temperature ranges for all silicas, though the temperatures and quantities of weight loss differ. In Figure 6, the differential weight losses of ZSM-5, silicalite-1, extracted nanoparticles, and (TPA)Br crystals are shown. It is clear that there are large shifts in the temperature range at which weight

TABLE 2: Weight Loss of Samples of TPA-Containing Silicalite-1, TPA-SBA-15, Extracted Nanoparticles, (TPA)OH, and (TPA)Br

sample	first wt loss		second wt loss	
	temp range (K)	wt loss (%)	temp range (K)	wt loss (%)
silicalite-1 (210 nm)	420–700	12.8	720–970	1.1
silicalite-1 (300 nm)	440–710	12.6	720–940	1.1
silicalite-1 (710 nm)	480–710	13.0	730–990	1.3
ZSM-5	545–685	8.7	685–900	1.3
nanoparticles 1, washed	365–540	33.2	550–830	5.2
nanoparticles 2, washed	395–545	14.1	565–735	3.9
nanoparticles 3	390–535	44.8	610–920	7.0
TPA-SBA-15	400–500	2.3	540–870	5.2
(TPA)OH in H ₂ O	300–345	85.6	360–400	10.6
(TPA)Br	450–500			

TABLE 3: BET Surface Areas for Silicalite-1, ZSM-5, and Extracted Nanoparticles as a Function of the Degassing Procedure

silica phase	pretreatment method ^a	BET surface area (m ² /g)
colloidal silicalite-1	513 K, overnight	36 ± 1
ZSM-5	513 K, overnight	66 ± 1
nanoparticles, as synthesized	413 K, overnight	33 ± 1
	513 K, overnight	597 ± 6
	513 K, 1 hour	968 ± 5
nanoparticles, washed with water	413 K, overnight	111 ± 2
	513 K, overnight	499 ± 9

^a The samples were kept in a vacuum at the given temperature for the specified amount of time.

loss occurs. For all silica phases, the first weight loss event is larger and occurs at a higher rate than that of the second weight loss event. (TPA)Br shows only one region of weight loss ((TPA)Cl shows exactly the same characteristics as (TPA)Br; (TPA)OH in water is decomposed completely below 400 K).

Table 2 summarizes the weight losses of various silica phases, (TPA)OH solution, and (TPA)Br crystals. The percentage of weight loss is taken with respect to the weight of the sample at ~950 K, thereby subtracting the weight losses of volatiles. The temperature ranges were identified by inspection of the differential weight loss curves. It is noteworthy that the first weight loss of the extracted nanoparticles occurs through a rather broad range, extending from the first weight loss of TPA-SBA-15 to the loss for (TPA)Br. A large variation in the weight loss is observed for different samples of the extracted nanoparticles which might be due to differences in the fraction of “excess” TPA removed during washing of the nanoparticles with water. In addition, no clear cutoff temperature exists at which the second weight loss event is over, a slight decline is visible up to 1070 K, which contributes less than 1 wt % of the total.

BET Surface Area. The surface area of the extracted nanoparticles as measured by nitrogen adsorption varies depending on the activation (degassing) procedure (see Table 3). Comparison is made with ~300 nm colloidal silicalite-1 particles and ZSM-5 crystals. It is important to realize that these samples are *not* calcined and therefore their internal pore structure is not accessible to nitrogen. Small external surfaces of 36 and 66 m²/g are measured for the silicalite-1 and ZSM-5 crystals, respectively. The surface area measured for extracted nanoparticles depends on the degassing temperature and the duration of degassing, whether the particles are washed with water. When degassing at 413 K overnight (below the temperature at which the first weight loss is observed with TGA), a total of 33 m²/g is measured. Washing out the excess TPA increases the surface area to 111 m²/g. Degassing overnight at 513 K, above the

temperatur at which the first weight loss is observed with TGA, results in higher surface areas: 597 and 499 m²/g for as-synthesized and washed particles, respectively. The surface area can be increased substantially by degassing the as-synthesized particles at 513 K for a very short time only (~1 h). Surface areas in the range 968–1240 m²/g are obtained, depending on the sample. These extremely high surface areas are unstable and if degassing is extended, the area decreases to the values obtained for degassing overnight. These large surface areas indicate that the extracted phase consists of nanoparticles that have agglomerated during the separation protocol. Analysis of the pore size distribution of the high surface-area materials using the BJH method reveals that the samples contain mostly mesopores of 4 nm or less in diameter.

Simulated Annealing of Particle Shape Determined by ²⁹Si MAS NMR Spectra. Figure 2a compares solutions from both of the simulated annealing strategies produced from initially random structures composed of 382–384 T-atoms. The upper diagrams are two different views of a structure simulated by the 12 T-atom building unit, which is highlighted in the graph. This structure displays typical average dimensions of particles simulated by the 12 T-atom building unit with a longer *c* dimension and comparable *a* and *b* dimensions (typical dimensions of the rodlike structures are 1.3 × 1.9 × 6.0 nm in the *a*, *b*, *c* directions, respectively). The depicted rodlike particles have the following *Qⁿ* fractions: 1.6% *Q¹*, 10.2% *Q²*, 40.1% *Q³*, and 48.7% *Q⁴*. The *Qⁿ* values used as targets for the simulated annealing are the ones reported by Ravishankar et al.²⁹ (0% *Q¹*, 8.3% *Q²*, 40.6% *Q³*, and 51.1% *Q⁴*), and therefore ~4% of the T-atoms in the system are in positions that do not fit the optimum. Yet, the differences between the expected values and the ones in the model are not much different from the error in the fitting of the ²⁹Si MAS NMR spectra.

Unlike the structures obtained above, nanoparticles determined using the single-silicon-atom building unit can have multiple shapes (i.e., there are multiple local minima that satisfy the objective function). The bottom images of Figure 2a display two different views of a structure simulated through the movement of SiO_{4/2} units on an MFI lattice and Figure 2b shows further possible morphologies from selected local minima. Structure B has 0.3% *Q⁰*, 0.3% *Q¹*, 7.1% *Q²*, 42.9% *Q³*, and 50.0% *Q⁴*, and structure C has 0.3% *Q⁰*, 0.3% *Q¹*, 6.8% *Q²*, 42.7% *Q³*, and 49.7% *Q⁴*. The difference between simulated and experimental *Q* values is comparable to the error in the NMR fitting. Typically, the *Q* values of well-optimized nanostructures obtained using the single silicon building unit fall within this range and some are within just one T-atom of the optimum structure. This slightly “better” agreement (again within experimental error) is due to the enhanced number of degrees of freedom in the single silicon case where the atoms are not united in a 12 T-atom cluster.

An easy way to quantify the difference in nanoparticle morphology found in the single-silicon building unit is through the particle dimensions. In Figure 2a, the single silicon simulation structure has a long *c* dimension that is comparable to all well-optimized structures formed using the 12-T atom building unit model. In contrast to the building block model, only about 50% of the models generated using the single silicon model exhibit a long axis along the *c* direction. An example is displayed in Figure 2b, where structures B and C have long *b* and *a* dimensions in contrast to structure A (with the long *c* dimension structure from Figure 2a). The significant variation in particle shape further emphasizes the limitations of the approach itself, i.e., basing particle structure solely on NMR spectra. In addition to displaying morphological variations, the

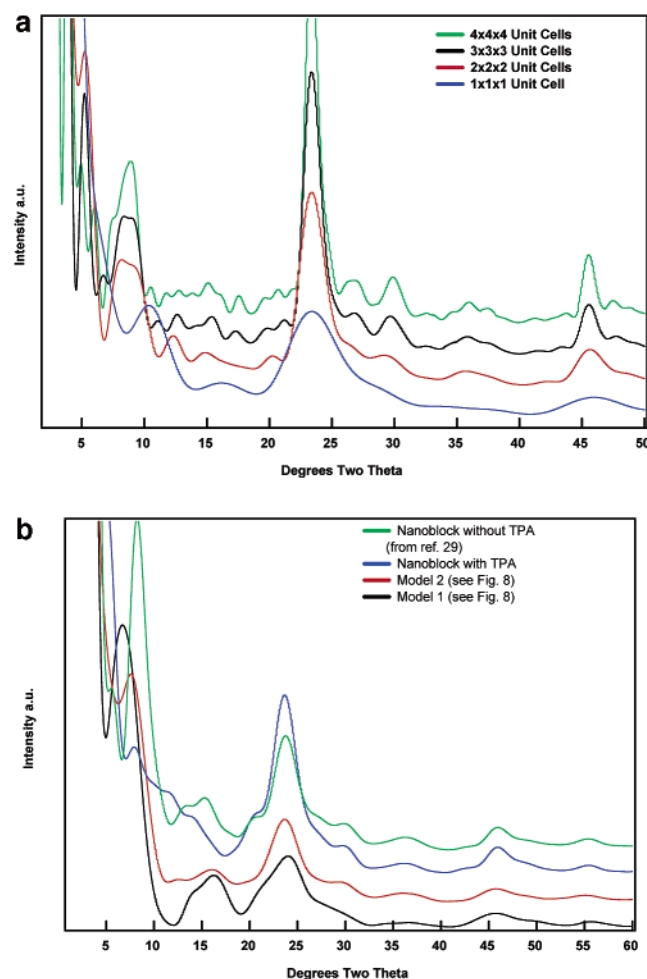


Figure 7. (a) Simulated XRD patterns of ultra-small TPA-containing silicalite-1 crystals of various particle dimensions (calculated using UDSKIP). (b) Simulated XRD patterns of the nanoblocks (with and without the TPA) and the nonperiodic structures obtained from the simulated annealing. These patterns were calculated using the Debye formula.

single silicon model differs from the 12 T-atom building unit in that the former accounts for internal defects. On average, single-silicon structures display $\sim 18\%$ internal defects.

When no internal defects are assumed, the slab structure proposed in ref 29 has Q values of 0% Q^1 , 11.1% Q^2 , 35.4% Q^3 , and 53.6% Q^4 resulting in $\sim 6\%$ T-atoms having an incorrect connectivity (i.e., larger than experimental error). This structure, along with rods and spheres, was also annealed with the 12 T-atom simulated annealing model to test the stability of such predefined structures. Annealing over shortened annealing schedules was used to ensure that the structures would not simply revert to a random arrangement. We have found that the annealed structures are rodlike, such as the ones displayed in Figure 2a, independent of the initial shape; i.e., the rodlike nanostructures appear to be the most stable when the 12 T-atom building unit is used.

Simulation of X-ray Diffraction Patterns. A large number of models were used to simulate the diffraction patterns of nanoparticles and nanosized crystals. For very small crystals ($1 \times 1 \times 1$ to $4 \times 4 \times 4$ unit cells; see Figure 7a) the two dominant features are broad peaks at $8\text{--}12^\circ 2\theta$ and at $24^\circ 2\theta$. The low-angle peak shifts to lower angles as the size of the crystal increases and eventually evolves into two peaks for crystals of $\sim 8 \times 8 \times 8$ unit cells or larger.

The Debye formula was used to simulate the XRD patterns

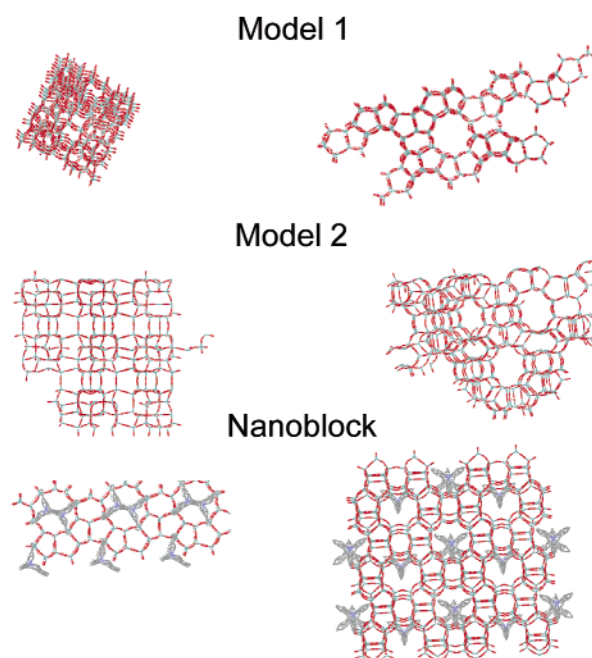


Figure 8. Illustration of the particles used for the simulations presented in Figure 7b.

of the nanoblocks reported in ref 29 and some of the structures obtained by the simulated annealing method (see Figure 7b). Although the relative intensity and position of the main features of the patterns changed slightly between the different models, all contain the two main features observed for the very small crystals of silicalite-1 calculated with UDSKIP. Note that the effect of the TPA in the model is to reduce the relative intensity of the peak at low angles. We thus surmise that if the samples of extracted nanoparticles are composed mainly of entities that resemble even roughly the structure of silicalite-1, we must observe the peak in the $8\text{--}10^\circ$ region. As is evident in Figure 3, the experimental pattern does not contain this feature and, thus, from the XRD alone we conclude that samples do not resemble the structure of silicalite-1.

Discussion

Nanoparticles were synthesized and extracted following a procedure reported in the literature. Confirmation that our final product is similar to that reported in the literature is provided by comparing our FTIR and ^{29}Si MAS NMR spectra and, to a lesser extent, our TGA data with literature reports.

The FTIR spectra of the extracted material appear identical to the one reported in ref 37. The observed position of the band characteristic of the pentasil ring is consistent with literature reports. For ZSM-5, we find a band at 540 cm^{-1} compared to a literature value of 550 cm^{-1} (note that the literature data is for calcined samples). For crystals in the colloidal range, we observe a doublet at 540 and 557 cm^{-1} ; literature values are 550 and 570 cm^{-1} .³¹ The extracted nanoparticles have a broad band at 565 cm^{-1} ; the literature value is 570 cm^{-1} .³⁷ Although we find a less pronounced blue shift ($\sim 10\text{ cm}^{-1}$) upon a decrease in the particle size in comparison with the literature, the trend is similar and approximately of the same order of magnitude. The solid-state ^{29}Si MAS NMR spectrum reveals the relative proportions of the silicon environments. Agreement with literature is within the error of the fitting method. We find relative proportions of the Q^1 , Q^3 , and Q^2 silicons of 50.2, 41.4, and 8.5% whereas literature reports 51.1, 40.6, and 8.3%, respectively.²⁹ From thermogravimetric analysis we obtain a

similar weight loss in the high-temperature range. Starting at about 550 K, we obtain a loss from 3.9 to 7.0%. The literature value is 6.6%, which falls within our range. It must be noted that this weight loss takes place over a large temperature range and has no clear cutoff.

Given the fact that we have followed the same preparation and separation protocols and that our FTIR, NMR, and TGA results are in good agreement with the literature, it appears that our samples are similar to the ones reported in refs 29 and 37.

During the extraction process, DLS indicates that the particles grow. It is likely that the particles grow by aggregation because Ostwald ripening is a much slower process. Although the stabilization mechanism of nanoparticles in solution is unclear, it is expected that if charge stabilization plays a role, both the acidification and extraction steps destabilize the particle suspension substantially. During the acidification, the particles go through the isoelectric point: silica is negatively charged at high pH and positively charged at low pH.^{73,74} At the isoelectric point, the stabilizing charge is absent. In the extraction step, both the lowered dielectric constant and screening effects from the addition of salt contribute to the collapse of the stabilizing electric double layer.^{75,76} The difficulty in redispersing the particles indicates that the nanoparticles are aggregated rather than flocculated. Even though the particles are aggregated, it is possible that their structure might be preserved during the extraction. Note that at all times the solutions appear transparent to the naked eye, and it may be concluded, incorrectly, that no aggregation has taken place.

Crystal structure information is usually best obtained with techniques that probe long range ordering such as X-ray diffraction. There is no lower limit to the crystal size to give rise to a diffraction pattern, though Bragg diffraction peaks do require a crystal with a few tens of unit cells to give rise to narrow peaks.⁴⁷ (Assertions to the contrary⁷⁷ have been demonstrated to be wrong by Schlenker and Peterson.⁴⁷) Our XRD pattern of the extracted nanoparticles appears very similar to that of amorphous silica (Figure 3). If these particles had a well-organized crystalline structure, as suggested in ref 29, the lack of distinct diffraction peaks observed experimentally can be attributed to their small nanoparticle size. To test this possibility, XRD simulations were conducted using UDSKIP. Note that TPA-silicalite-1 has a well-defined crystal structure, $[(C_{12}N)_4(Si_96O_{192})]$, with unit cell of dimensions $a = 20.022$, $b = 19.899$, and $c = 13.383$ Å.⁷⁸ Using the Debye formula, a section of this crystal structure was simulated (see Figure 7b), as this is the proposed nanoparticle structure in ref 29.

Parts a and b of Figure 7 show the simulated X-ray diffraction patterns for nanoparticles of TPA-silicalite-1 of different dimensions and those for the nanoparticles structures proposed in ref 29 and called *nanoblocks* (based on TPA-silicalite-1). TPA-silicalite-1 clearly shows distinct peaks even for crystals as small as 1 or $2 \times 2 \times 2$ unit cells. The diffraction peaks of crystalline nanoparticles are, of course, considerably broadened and shifted from the positions of the peaks of larger crystals. (The peaks observed at very low angles arise from intensity enhancement of the wings of the interference function by the Lorentz polarization factor.^{44,47}) Since silicalite-1 crystals comparable in size to the nanoparticles should give rise to X-ray diffraction, it is concluded that the extracted nanoparticles possess neither the MFI framework structure, nor other well-defined internal structure. The diffraction patterns strongly suggest that the particles are disordered and resemble the local structure of amorphous silica.

Ravishankar et al.²⁹ carried out an analysis of the ²⁹Si MAS

NMR spectra of the extracted nanoparticles to obtain the particle shape and size that better fits the experimental data. A selected group of shapes (cubes, rods, and plates of different aspect ratio) containing no internal defects were examined. Although ²⁹Si MAS NMR provides the fractions of different coordination environments of silicons, it is important to realize that even a highly crystalline TPA-silicalite-1 sample has internal silanol groups to compensate for the charge of the TPA cation and these can amount to ~17% of the area under the peaks (by accounting for four Q³ per TPA).⁵⁵ In the calculations of Ravishankar et al.,²⁹ the effect of these internal defects on the ²⁹Si NMR spectrum has been ignored. The large fraction of Q³ and Q² silicons in the extracted nanoparticles may point to other types of internal defects⁷⁹ (arising from an incompletely formed framework) that have also not been included in the calculations of Ravishankar et al.²⁹

Following the simulated annealing approach described above, we have found structures whose Qⁿ values are within the experimental error of our ²⁹Si NMR data. Due to its statistical nature and exploration of parameter space, more than one structure can generally describe the experimental data well. (This is indicative of the lack of sufficient information in the NMR spectrum alone to precisely provide a single structure.) Structures obtained using a 12 T-atom building block exhibit shape variations but are primarily rods. In particular, most (above 75% of the final structures regardless of the initial and final temperatures) of the 12 T-atom simulations have an elongated morphology along the *c* crystal dimension, and short *a* and *b* dimensions. The single SiO_{4/2} building unit structures display a greater variety of shapes and different dominant dimensions of the nanoparticles. SiO_{4/2} building block simulations lead to open structures with no well-defined shapes and approximately 15% internal Q³s or Q²s. The sizes are normally less than 6 nm in the longest dimension and at least 1.3 nm in the shortest dimension. These structures are very open and thus contain many defects. The size of the structures obtained is in the range of a few nanometers, in agreement with the size of nanoparticles in solution as reported in the literature.²⁷ Our method of simulation is much more general than the methodology of ref 29 where the NMR data were fitted with pre-assumed shapes of varying dimensions (even if we accept that the particles have the structure of silicalite-1). Our results indicate that other particle shapes (*not* the proposed slab shape) are the most likely candidates on the basis of the NMR data.

A recent publication by the same group³⁶ reported the in situ ²⁹Si NMR spectrum of a liquid sample containing the nanoblocks. This spectrum is substantially different from the one that is obtained for the extracted nanoparticles: it contains no detectable fraction of Q⁴. The broad signals are attributed to "particle-like" species: however, a 3 nm particle has a rotational correlation time of $\tau \sim 0.2 \mu s$ ⁸⁰ at 300 K, which is well within the range in which rapid particle motion should lead to well-defined peaks (that is, if the structure is well-defined).⁸⁰ The peak broadening is thus more likely the result of an underlying disordered structure. Moreover, the differences between the spectra of the in situ and ex situ samples indicate that major changes in connectivity within the particles have occurred during the extraction process. It is therefore unwarranted to extrapolate conclusions about the structure of the nanoparticles in solution from data obtained from the extracted product.

Determination of the location of TPA is a rather difficult question to address. TPA could be present as a bulk phase between the particles, or adsorbed to the surface, or even incorporated in the particles. ¹³C CPMAS NMR and FTIR

indicate the presence of TPA but fail to provide information about the location. Extraction of the particles leaves a significant amount of TPA in a bulklike phase that can partly be removed by washing with water, as evident from TGA. Note that in the TGA there are weight loss events at two temperature ranges. The first range, from about 365 to 545 K, is rather broad and overlaps with the weight losses of (TPA)Br and the first weight loss of TPA-SBA-15. During extraction, a large amount of HCl and NaCl are added that could form (TPA)Cl crystals, explaining the overlap with (TPA)Br. TPA-SBA-15 has amorphous walls and exhibits a very high surface area. It is likely that part of the TPA adsorbs on the surface and gives rise to a low-temperature weight loss. Therefore, we assign the first loss of the nanoparticles partly to TPA adsorbed on the surface and/or partly to the presence of (TPA)Cl. A second weight loss occurs at much higher temperatures: between about 550 and 920 K. The range is not well-defined and starts at the end of the first weight loss observed for well-formed microporous silicas such as colloidal silicalite-1 and ZSM-5. For these porous silicas this weight loss is attributed to TPA occluded in channel intersections. For TPA-SBA-15, weight loss takes place at very similar temperatures. The higher temperatures needed for the weight loss and the less defined range could be explained by TPA incorporated inside the particles at sites that are less accessible than the pores of the ZSM-5 framework. Comparison of our TGA data for the extracted nanoparticles and the TPA-SBA-15 indicates that some of the TPA in the case of nanoparticles is incorporated in an amorphous phase.

The strong dependence of the BET surface area on the degassing procedure can be understood from the TGA data. Degassing at temperatures below the first weight loss leaves TPA adsorbed on the surface and associated with chloride as (TPA)Cl. This forms a bulklike condensate between the particles, giving rise to a very low surface area. Degassing above the first weight loss removes the bulklike condensate, increasing the BET surface. The duration of the degassing affects the surface enormously. Short degassing (~ 1 h) results in extremely high surface areas of around 1000 m²/g. Extending the degassing decreases the surface area. A rationale could be provided by the condensation of extremely small particles to form aggregates during the degassing. When a density is assumed in the range of TPA-MFI (1.99 g/mL) and amorphous silica (2.2–2.5 g/mL), surfaces of around 1000 m²/g require particles sizes in the range of a few nanometers.

Despite the great intuitive appeal of a well-defined structure of the precursor subcolloidal nanoparticles in the synthesis of silicalite-1, the evidence provided here does not support their existence. Although we cannot exclude the possibility that the nanoparticles present in the TPA-silica solution have a structure related to silicalite-1, we provide clear evidence that the extracted nanoparticles do not possess such a structure. It is noteworthy that Kirschhock et al.^{32–34} have built a new paradigm for the formation of silicalite-1 on the basis of the presumed existence of these well-structured nanoblocks.^{32–36} Our work adds further weight to the criticisms of Knight and Kinrade⁸¹ regarding their NMR investigations. TEM and AFM studies to be reported elsewhere⁸² are also in sharp contrast to the TEM and AFM findings of refs 29 and 35. The conclusions that have been drawn on the basis of the *nanoblock* model must be considered questionable until further evidence or reevaluation of the experimental data of the extracted powder is given.

Summary and Conclusions

Subcolloidal nanoparticles were synthesized by a clear solution method and extracted following a procedure proposed in the literature. The dried particles were studied with a range of experimental and simulation techniques in an attempt to clarify their structure and morphology. The rationale is that the particles are preserved during the extraction method. Comparison of experimental and simulated XRD patterns suggests that the extracted particles are amorphous. TGA indicates that these amorphous particles likely incorporate TPA, though they are separated by a bulklike TPA-condensate. Modeling of the ²⁹Si MAS NMR spectra using simulated annealing reveals nanoparticles with a range of open shapes and a considerable fraction of internal defects. In contrast to previous suggestions, it is clear that the extracted nanoparticles do not have a well-defined shape. While extracted nanoparticles appear to have a size similar to that in solution (based on BET data), it is still unclear whether the extraction procedure preserves at least the structure of the nanoparticles. In situ experiments together with simulations are needed to address this question and these will be the subject of future work.

Acknowledgment. This work was funded from NSF-Nanoscale Interdisciplinary Research Team (NIRT) grant CTS0103010. We thank I. Peral for fruitful discussions about the XRD patterns and J.H.D. Boshoff for providing the UDSKIP code. E. W. Kaler and N. J. Wagner are acknowledged for use of the DLS equipment. We thank R. J. Accardi for acquiring some of the NMR spectra. We are grateful to the Department of Chemistry and Biochemistry at the University of Delaware for use of the NMR facilities and C. Dybowski and S. Bai for useful discussions. We thank Dr. Ravishankar for advice on the extraction procedure at the early stages of this project.

References and Notes

- (1) Ying, J. Y.; Mehnert, C. P.; Wong, M. S. *Angew. Chem., Int. Ed.* **1999**, *38*, 56.
- (2) Cambor, M. A.; Villaescusa, L. A.; Diaz-Cabanas, M. J. *Top. Catal.* **1999**, *9*, 59.
- (3) Heywood, B. R.; Mann, S. *Adv. Mater.* **1994**, *6*, 9.
- (4) Mann, S.; Burkett, S. L.; Davis, S. A.; Fowler, C. E.; Mendelson, N. H.; Sims, S. D.; Walsh, D.; Whilton, N. T. *Chem. Mater.* **1997**, *9*, 2300.
- (5) Mann, S. *Nature* **1988**, *332*, 119.
- (6) Vrieling, E. G.; Beelen, T. P. M.; van Santen, R. A.; Gieskes, W. W. C. *J. Biotechnol.* **1999**, *70*, 39.
- (7) Climent, M. J.; Velt, A.; Corma, A. *Green Chem.* **2002**, *4*, 565.
- (8) Corma, A.; Diaz-Cabanas, M.; Martinez-Triguero, J.; Rey, F.; Rius, J. *Nature* **2002**, *418*, 514.
- (9) Lee, G. S.; Nakagawa, Y.; Hwang, S. J.; Davis, M. E.; Wagner, P.; Beck, L.; Zones, S. I. *J. Am. Chem. Soc.* **2002**, *124*, 7024.
- (10) Corma, A.; Navarro, M. T.; Rey, F.; Valencia, S. *Chem. Commun.* **2001**, 1486.
- (11) Marler, B.; Werthmann, U.; Gies, H. *Micropor. Mesopor. Mater.* **2001**, *43*, 329.
- (12) Zones, S. I.; Nakagawa, Y.; Lee, G. S.; Chen, C. Y.; Yuen, L. T. *Micropor. Mesopor. Mater.* **1998**, *21*, 199.
- (13) Zones, S. I.; Nakagawa, Y.; Yuen, L. T.; Harris, T. V. *J. Am. Chem. Soc.* **1996**, *118*, 7558.
- (14) Burkett, S. L.; Davis, M. E. *J. Phys. Chem.* **1994**, *98*, 4647.
- (15) Burkett, S. L.; Davis, M. E. *Chem. Mater.* **1995**, *7*, 1453.
- (16) Burkett, S. L.; Davis, M. E. *Chem. Mater.* **1995**, *7*, 920.
- (17) Davis, M. E.; Lobo, R. F. *Chem. Mater.* **1992**, *4*, 756.
- (18) Schoeman, B. J.; Sterte, J.; Otterstedt, J. E. The Synthesis of Discrete Colloidal Zeolite Particles. In *Zeolites and Microporous Crystals*; 1994; Vol. 83, p 49.
- (19) Schoeman, B. J.; Regev, O. *Zeolites* **1996**, *17*, 447.
- (20) Schoeman, B. J. *Micropor. Mesopor. Mater.* **1998**, *22*, 9.
- (21) Nikolakis, V.; Kokkoli, E.; Tirrell, M.; Tsapatsis, M.; Vlachos, D. G. *Chem. Mater.* **2000**, *12*, 845.
- (22) Watson, J. N.; Iton, L. E.; White, J. W. *Chem. Commun.* **1996**, 2767.

- (23) Watson, J. N.; Iton, L. E.; Keir, R. I.; Thomas, J. C.; Dowling, T. L.; White, J. W. *J. Phys. Chem. B* **1997**, *101*, 10094.
- (24) Watson, J. N.; Brown, A. S.; Iton, L. E.; White, J. W. *J. Chem. Soc., Faraday Trans.* **1998**, *94*, 2181.
- (25) de Moor, P.; Beelen, T. P. M.; Komanschek, B. U.; Diat, O.; van Santen, R. A. *J. Phys. Chem. B* **1997**, *101*, 11077.
- (26) de Moor, P.; Beelen, T. P. M.; Komanschek, B. U.; van Santen, R. A. *Micropor. Mesopor. Mater.* **1998**, *21*, 263.
- (27) de Moor, P.; Beelen, T. P. M.; van Santen, R. A.; Tsuji, K.; Davis, M. E. *Chem. Mater.* **1999**, *11*, 36.
- (28) de Moor, P.; Beelen, T. P. M.; van Santen, R. A.; Beck, L. W.; Davis, M. E. *J. Phys. Chem. B* **2000**, *104*, 7600.
- (29) Ravishankar, R.; Kirschhock, C. E. A.; Knops-Gerrits, P. P.; Feijen, E. J. P.; Grobet, P. J.; Vanoppen, P.; De Schryver, F. C.; Mieke, G.; Fuess, H.; Schoeman, B. J.; Jacobs, P. A.; Martens, J. A. *J. Phys. Chem. B* **1999**, *103*, 4960.
- (30) Ravishankar, R.; Martens, J. A.; Jacobs, P. A. *Micropor. Mater.* **1997**, *8*, 283.
- (31) Ravishankar, R.; Kirschhock, C.; Schoeman, B. J.; Vanoppen, P.; Grobet, P. J.; Storck, S.; Maier, W. F.; Martens, J. A.; De Schryver, F. C.; Jacobs, P. A. *J. Phys. Chem. B* **1998**, *102*, 2633.
- (32) Kirschhock, C. E. A.; Ravishankar, R.; Jacobs, P. A.; Martens, J. A. *J. Phys. Chem. B* **1999**, *103*, 11021.
- (33) Kirschhock, C. E. A.; Ravishankar, R.; Verspeurt, F.; Grobet, P. J.; Jacobs, P. A.; Martens, J. A. *J. Phys. Chem. B* **1999**, *103*, 4965.
- (34) Kirschhock, C. E. A.; Ravishankar, R.; Van Looveren, L.; Jacobs, P. A.; Martens, J. A. *J. Phys. Chem. B* **1999**, *103*, 4972.
- (35) Kirschhock, C. E. A.; Buschmann, V.; Kremer, S.; Ravishankar, R.; Houssin, C. J. Y.; Mojet, B. L.; van Santen, R. A.; Grobet, P. J.; Jacobs, P. A.; Martens, J. A. *Angew. Chem., Int. Ed.* **2001**, *40*, 2637.
- (36) Kirschhock, C. E. A.; Kremer, S. P. B.; Grobet, P. J.; Jacobs, P. A.; Martens, J. A. *J. Phys. Chem. B* **2002**, *106*, 4897.
- (37) Ravishankar, R.; Kirschhock, C. E. A.; Schoeman, B. J.; de Vos, D.; Grobet, P. J.; Jacobs, P. A.; Martens, J. A. "Synthesis, Isolation and Characterization of Nano-Powder of Silicalite-1 Type Molecular Sieves"; 12th International Zeolite Conference, 1998, Baltimore, MD.
- (38) Rieger, J.; Horn, D. *Angew. Chem., Int. Ed.* **2001**, *40*, 4330.
- (39) Lovallo, M. C.; Gouzinis, A.; Tsapatsis, M. *AIChE J.* **1998**, *44*, 1903.
- (40) Kruk, M.; Jaroniec, M.; Ko, C. H.; Ryoo, R. *Chem. Mater.* **2000**, *12*, 1961.
- (41) Zhao, D. Y.; Huo, Q. S.; Feng, J. L.; Chmelka, B. F.; Stucky, G. D. *J. Am. Chem. Soc.* **1998**, *120*, 6024.
- (42) Zhao, D. Y.; Feng, J. L.; Huo, Q. S.; Melosh, N.; Fredrickson, G. H.; Chmelka, B. F.; Stucky, G. D. *Science* **1998**, *279*, 548.
- (43) Sawant, K. R.; Lobo, R. F. *Chem. Mater.*, submitted for publication.
- (44) Warren, B. E. *X-ray Diffraction*, reprint ed.; Dover Publications Inc.: Toronto, Ontario, 1990.
- (45) Waasmaier, D.; Kirfel, A. *Acta Crystallogr. Sect. A* **1995**, *51*, 416.
- (46) Boshoff, J. UDSKIP: Powder Diffraction Patterns from Ultrasmall Zeolite Crystals; 1.1 ed., 2003.
- (47) Schlenker, J. L.; Peterson, B. K. *J. Appl. Crystallogr.* **1996**, *29*, 178.
- (48) Our implementation of the algorithm by Schlenker et al. is called UDSKIP and can be obtained at http://www.che.Udel.edu/research_groups/nanomodelling/resources.html
- (49) Kirkpatrick, S.; Gelatt, C. D.; Vecchi, M. P. *Science* **1983**, *220*, 671.
- (50) Allen, M. P.; Tildesley, D. J. *Computer Simulation of Liquids*; Oxford Science Publications: New York, 1987.
- (51) Goffe; Ferrier; Rogers. *J. Econometrics* **1994**, *60*, 65.
- (52) Keen, D. *Phase Transitions* **1997**, *61*, 109.
- (53) McGreevy, R. L. *J. Phys. Condens. Matter* **2001**, *13*, 877.
- (54) Engelhardt, G. Solid State NMR Spectroscopy Applied to Zeolites. In *Introduction to Zeolite Science and Practice*, 2nd ed.; van Bekkum, H., Flanigen, E. M., Jacobs, P. A., Jansen, J. C., Eds.; Elsevier: Amsterdam, 2001; Vol. 137.
- (55) Koller, H.; Lobo, R. F.; Burkett, S. L.; Davis, M. E. *J. Phys. Chem.* **1995**, *99*, 12588.
- (56) Shantz, D. F.; Lobo, R. F. *Chem. Mater.* **1998**, *10*, 4015.
- (57) Shantz, D. F.; Fild, C.; Koller, H.; Lobo, R. F. *J. Phys. Chem. B* **1999**, *103*, 10858.
- (58) Shantz, D. F.; auf der Gunne, J. S.; Koller, H.; Lobo, R. F. *J. Am. Chem. Soc.* **2000**, *122*, 6659.
- (59) Scarano, D.; Zecchina, A.; Bordiga, S.; Geobaldo, F.; Spoto, G.; Petrini, G.; Leofanti, G.; Padovan, M.; Tozzola, G. *J. Chem. Soc., Faraday Trans.* **1993**, *89*, 4123.
- (60) Jentils, A.; Lercher, J. A. Techniques of zeolite characterization. In *Introduction to Zeolite Science and Practice*, 2nd ed.; van Bekkum, H., Flanigen, E. M., Jacobs, P. A., Jansen, J. C., Eds.; Elsevier: Amsterdam, 2001; Vol. 137, p 345.
- (61) Knozinger, H.; Mestl, G. *Top. Catal.* **1999**, *8*, 45.
- (62) Bauer, F.; Geidel, E.; Peuker, C.; Pilz, W. *Zeolites* **1996**, *17*, 278.
- (63) Buge, H. G.; Peuker, C.; Pilz, W.; Jahn, E.; Rademacher, O. *Z. Phys. Chem.-Leipzig* **1990**, *271*, 881.
- (64) Jansen, J. C.; Vandergaag, F. J.; Vanbekkum, H. *Zeolites* **1984**, *4*, 369.
- (65) Zecchina, A.; Bordiga, S.; Spoto, G.; Scarano, D.; Petrini, G.; Leofanti, G.; Padovan, M.; Arean, C. O. *J. Chem. Soc., Faraday Trans.* **1992**, *88*, 2959.
- (66) Ugliengo, P.; Bleiber, A.; Garrone, E.; Sauer, J.; Ferrari, A. M. *Chem. Phys. Lett.* **1992**, *191*, 537.
- (67) Gutmann, V.; Resch, G.; Linert, W. *Coord. Chem. Rev.* **1982**, *43*, 133.
- (68) Konijnendijk, W. L.; Stevels, J. M. *J. Non-Cryst. Solids* **1976**, *20*, 193.
- (69) Bremard, C.; Laureyns, J.; Patarin, J. *J. Raman Spectrosc.* **1996**, *27*, 439.
- (70) Dutta, P. K.; Puri, M. *J. Phys. Chem.* **1987**, *91*, 4329.
- (71) Contreras, J. G.; Seguel, G. *Spectrosc. Lett.* **1981**, *14*, 553.
- (72) Harmon, K. M.; Bulgarella, J. A. *J. Mol. Struct.* **1995**, *351*, 181.
- (73) Dove, P. M.; Rimstidt, J. D. Silica-Water Interactions. In *Silica: Physical Behavior, Geochemistry and Materials Applications*; Heaney, P. J., Prewitt, C. T., Gibbs, G. V., Eds.; Mineralogical Society of America: Washington DC, 1994; Vol. 29, p 259.
- (74) Nikolakis, V.; Tsapatsis, M.; Vlachos, D. G. *Langmuir* **2003**, in press.
- (75) Hunter, R. J. *Introduction to Modern Colloid Science*, 1st ed.; Oxford University Press: Oxford, U.K., 1993.
- (76) Israelashvili, J. N. *Intermolecular and Surface Forces*, 2nd ed.; Academic Press: London, 1992.
- (77) Jacobs, P. A.; Derouane, E. G.; Weitkamp, J. *J. Chem. Soc., Chem. Commun.* **1981**, 591.
- (78) Vankoningsveld, H.; Vanbekkum, H.; Jansen, J. C. *Acta Crystallogr. Sect. B-Struct. Sci.* **1987**, *43*, 127.
- (79) Bordiga, S.; Roggero, I.; Ugliengo, P.; Zecchina, A.; Bolis, V.; Artioli, G.; Buzzoni, R.; Marra, G.; Rivetti, F.; Spano, G.; Lamberti, C. *J. Chem. Soc., Dalton Trans.* **2000**, 3921.
- (80) Mayer, C. *Prog. NMR Spectrosc.* **2002**, *40*, 307.
- (81) Knight, C. T.; Kinrade, S. D. *J. Phys. Chem. B* **2002**, *106*, 3329.
- (82) Ramanan, H.; Kokkoli, E.; Tsapatsis, M. Manuscript in preparation.